Electronic Supplementary Information

Fabrication of ultrathin single-layer 2D metal-organic framework nanosheets with excellent adsorption performance via a facile exfoliation approach

Lei-Lei Liu[a],*, Jing Chen[c,e], Yan Zhang[c,e], Cai-Xia Yu[a], Wei Du[a], Xue-Qin Sun[a], Jiang-Lou Zhang[c], Fei-Long Hu[d], Yan Mi[d],*, Lu-Fang Ma[b],*

[a] *School of Environmental and Material Engineering, Yantai University, Yantai 264005, P. R. China*

[b] *College of Chemistry and Chemical Engineering, Luoyang Normal University, Luoyang 471934, P. R. China*

[c] *College of Chemistry and Chemical Engineering, Anyang Normal University, Anyang 455000, P. R. China*

[d] *Guangxi Key Laboratory of Chemistry and Engineering of Forest Products, Guangxi University for Nationalities, Nanning 530006, P. R. China*

[e] *College of Chemistry and Molecular Engineering, Zhengzhou University, Zhengzhou 450001, P. R. China*

Experimental Section

General Procedure. 3-[(4-hydroxyphenyl)diazenyl]benzoic acid was prepared according to the literature method.[1] All other chemicals and reagents were obtained from commercial sources and used as received. ^{1}H NMR and ^{13}C NMR spectra were recorded at ambient temperature with a Bruker Avance III-400 spectrometer. Powder X-ray diffraction (PXRD) was performed using a PANalytical X'Pert PRO MPD system (PW3040/60). Thermal analysis was performed with a Netzsch STA-449F3 thermogravimetric analyzer at a heating rate of 10 °C min^{-1} and a flow rate of 20 cm^3 min^{-1} (N$_2$). The energy-dispersive X-ray spectroscopy (EDS) was recorded with a Bruker XFlash 6130 system at 15 kV. The zeta potential was determined using dynamic light scattering (DLS) on Malvern Instruments Nanosizer-ZS.

CR sorption studies. The aqueous solutions of CR with different concentrations were obtained by diluting the stock CR solution with the proper amount of distilled water unless otherwise indicated. The solution pH levels were adjusted by HCl or NaOH aqueous solution. The stirring speed was set at 2000 rpm. All adsorption tests were conducted at 298 K using 10 mg of adsorbent and 60 mL of CR standard solution, except that the adsorption isotherm studies were performed in 120 mL of CR standard solution, owing to that the ultrahigh concentration of CR leads to a great reduction of the accuracy in absorbance measurement.

For isotherm studies, 10 mg adsorbent was added into 120 mL CR solutions with different concentrations in a flask under continuous stirring to reach adsorption equilibrium. For kinetic studies, a typical adsorption experiment (10 mg of adsorbent) was performed under continuous stirring at the obtained optimum pH value (pH = 3.5) for certain concentration CR (60, 150, and 300 ppm; 60 mL) solution. Analytical samples were taken from the mixed solution at given time intervals and immediately separated by centrifugation. The residual concentrations of CR in the solution were measured by Varian 50 UV-vis spectrophotometer at the maximum absorbance of CR (560 nm). The amount of dye adsorbed on the adsorbent q_t (mg g^{-1}) and the removal efficiency were obtained from the following equations:

$$q_t = \frac{(C_0 - C_t)V}{m} \tag{1}$$

$$Removal\ efficiency\ (\%) = \frac{C_0 - C_e}{C_0} \times 100\% \tag{2}$$

Where C_0 (mg L^{-1}) and C_e (mg L^{-1}) are the initial and equilibrium concentrations of CR in the solution, respectively. V (L) is the volume of the solution, m (g) is the mass of the dry adsorbent.

The Langmuir, Freundlich and Dubinin-Radushkevich (D-R) isotherm models were employed to simulate the adsorption isotherm data, which can be described as follows:

$$\frac{C_e}{q_e} = \frac{C_e}{q_{m,L}} + \frac{1}{q_{m,L}K_L} \tag{3}$$

$$lnq_e = lnK_F + \frac{1}{n}lnC_e \qquad \text{(4)}$$

$$lnq_e = lnq_{m,D-R} - k_{D-R}\varepsilon^2 \qquad \text{(5)}$$

Where q_e (mg g^{-1}) is the adsorption amounts at equilibrium and C_e (mg L^{-1}) is the equilibrium concentration of dyes. $q_{m,L}$ (mg g^{-1}) and $q_{m,D-R}$ (mg g^{-1}) are the maximum adsorption capacity of Langmuir and D-R isotherm models, respectively. K_L (L mg^{-1}) is the Langmuir constant. K_F ((mg g^{-1})/(mg L^{-1})$^{-1/nF}$) is the Freundlich constant, $1/n_F$ is the heterogeneity factor. k_{D-R} (mol^2 J^{-2}) is adsorption energy of D-R model, ε is Polanyi adsorption potential energy (ε = RTln(1+1/C_e)), E (kJ mol^{-1}) is an average free energy. The equilibrium adsorption energy E (E = (2k)$^{-0.5}$) value calculated by D-R adsorption isotherm model is very important. It can be used to judge the adsorption mechanism. It is considered that if the value of E lying between 8 and 16 kJ mol^{-1}, then the adsorption reaction occurs by ion exchange process; if E < 8 kJ mol^{-1}, the adsorption process is mainly a physical adsorption and if E > 16 kJ mol^{-1}, then the adsorption is dominated by chemical process.

The adsorption kinetics data were fitted with pseudo-second-order, which expressed as follows:

$$\frac{t}{q_t} = \frac{1}{k_2 q_e^2} + \frac{t}{q_e} \qquad \text{(6)}$$

where k_2 (g mg^{-1} min^{-1}) is kinetic rate constant for the pseudo-second-order model; q_t (mg g^{-1}) is the adsorption capacity at any time t (min); q_2 (mg g^{-1}) is the theoretical value for the adsorption capacity.

Rhodamine 6G (R6G), rhodamine B (RhB) and fluorescein (FO) were selected to study the selective adsorption of CR. The MOF nanosheets (10 mg) was stirred with the solutions of CR&R6G (180/10 ppm), CR&RhB (90/10 ppm), CR&FO (60/20 ppm) and CR&R6G&RhB&FO (180/10/10/20 ppm) in flakes, respectively. The dyes adsorption processes were recorded over given time intervals by measuring UV-vis absorption spectra of the dye mixtures.

The isotherm adsorption for anionic dyes of methyl orange (MO), acid orange G (AO) and acid red 29 (AR) are performed as following: at optimum pH value (pH = 3.5), 10 mg adsorbent was added into 60 mL dyes solutions with different concentrations in a flask under continuous stirring to reach adsorption equilibrium. At given time intervals, analytical samples were taken from the mixed solution and immediately separated by centrifugation. The mixed anionic dyes of CR (60 ppm), MO (30 ppm), AO (30 ppm) and AR (30 ppm) in 60 mL (pH = 3.5) solution was stirred with 10 mg adsorbent. The dyes adsorption processes were recorded over time intervals by measuring UV-vis absorption spectra of the dye mixtures.

Before the desorption test, 150 mg of the adsorbent was added in to 150 ml of CR solution (300 ppm). After reaching adsorption equilibrium, the CR loaded adsorbent was immersed in 50 mL of DMF in a flask at 298 K (24 h) for desorption. Then it was washed with DMF and dried in a vacuum oven.

X-ray crystal structure determination. Single X-ray diffraction of crystal was collected on a CCD diffractometer at 223 K. All diffractometers were equipped with a graphite monochromated Mo-Kα radiation (λ = 0.71073). The structure was solved by direct method and expanded with Fourier technique. All calculations were performed with SHELXL-97 package.[2] All H atoms in **Zn-MOF** were placed in geometrically idealized positions and constrained to ride on their parent atoms. Moreover, the diffused electron densities resulting from these residual solvent molecules were removed from the data set using the SQUEEZE routine of PLATON and refined further using the data generated.[3] The formula of $\{[Zn_2(5\text{-}OH\text{-}BDC)_2L_2]\cdot1.5H_2O\}_n$ was derived from thermogravimetric characterization. The crystal data for **Zn-MOF** was summarized as follows: $C_{66}H_{48}N_8O_{16}Zn_2$, Mr = 1339.91, monoclinic, space group $P2_1/c$, a = 19.727(4) Å, b = 14.139(3) Å, c = 30.256(6) Å, α = 90°, β = 105.25(3)°, γ = 90°, V = 8142(3) Å^3, Z = 4, D_c = 1.093 g cm^{-3}, $F(000)$ = 2752 and μ = 0.648 mm^{-1}, 65442 reflections collected, 14314 unique (R_{int} = 0.0844). R_1 = 0.0614, wR_2 = 0.1942 and S = 1.007. Crystallographic data have been submitted to the Cambridge Structural Database with deposition number CCDC 1888890.

SEM, TEM and AFM characterizations. Prior to the characterizations of scanning electron microscopy (SEM), transmission electron microscopy (TEM) and atomic force microscopy (AFM) characterizations, the suspension of 2D nanosheets was dropped onto the Si/SiO$_2$, holey carbon-coated carbon support copper grids and Si/SiO$_2$ or mica, respectively, and then naturally dried in air. SEM images were observed by the Hitachi SU8010 apparatus working at an acceleration voltage of 1/3 kV. TEM images were operated at an acceleration voltage of 200 kV (JEOL JEM 2100). AFM images were obtained on a dimension edge microscope (Bruker Edge) equipped with a tapping mode.
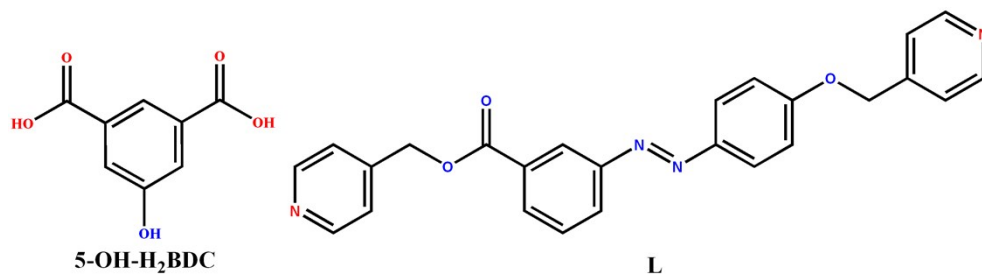
Scheme S1. Molecular structures of 5-OH-H₂BDC and L ligand.
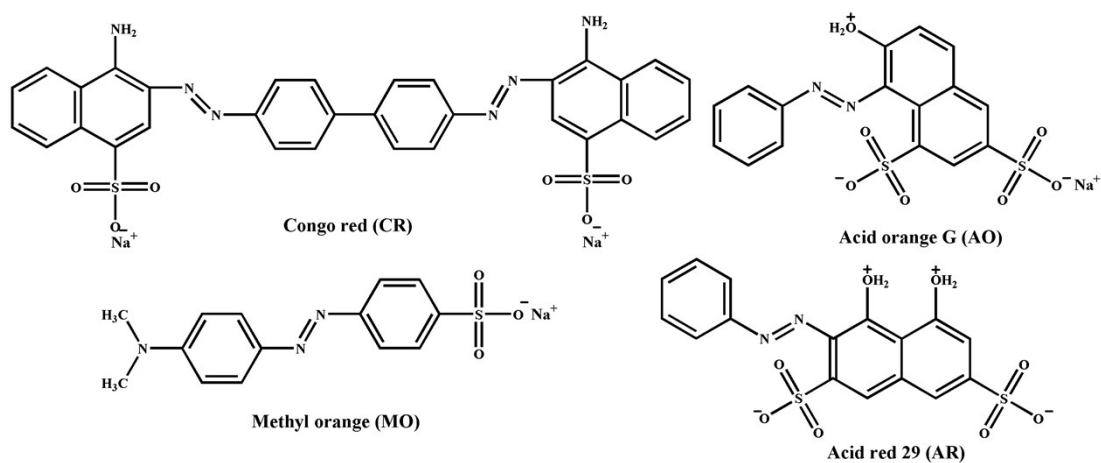
Scheme S2. Molecular structures of the anionic dyes in the acidic condition (pH = 3.5).
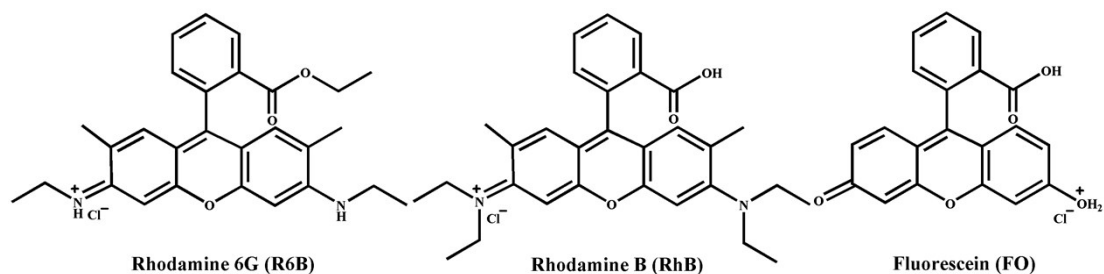
Scheme S3. Molecular structures of the non-anionic dyes in the acidic condition (pH = 3.5).
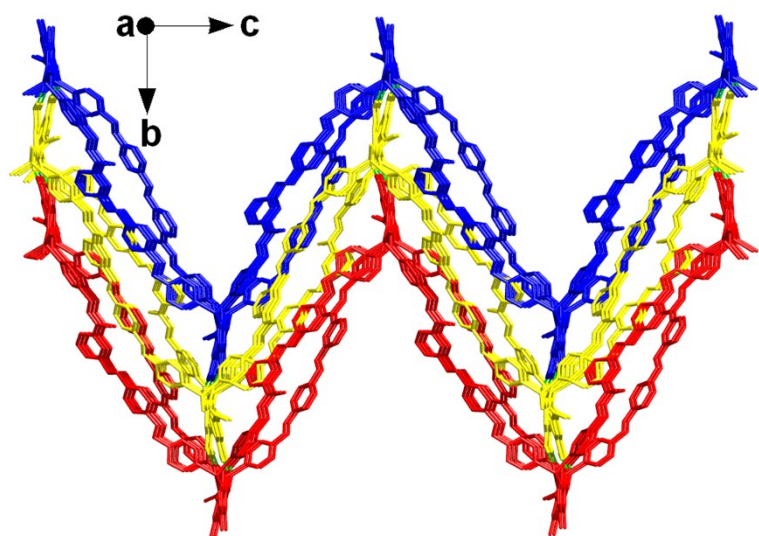
Figure S1. View of the O−H···O (O5–H5A···O3, 2.697 Å; O10–H10···O6, 2.646 Å) hydrogen bonds (green dashed lines) in **Zn-MOF**. All H atoms except those related to H-bonding interactions are omitted for clarity.
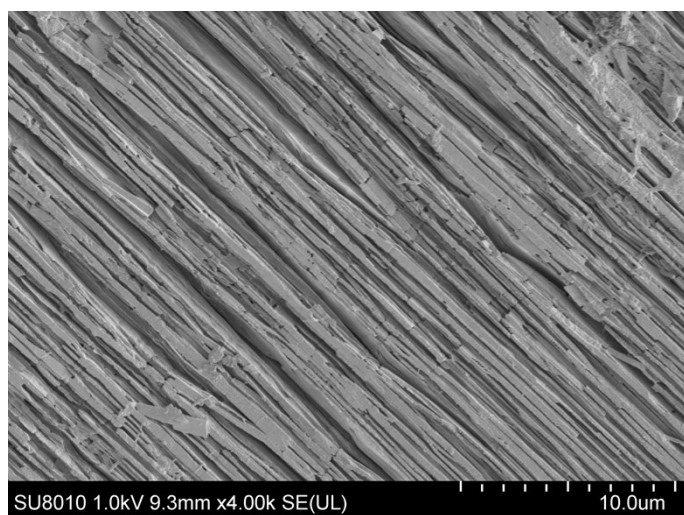
Figure S2. SEM image of the cross-section for **Zn-MOF**.
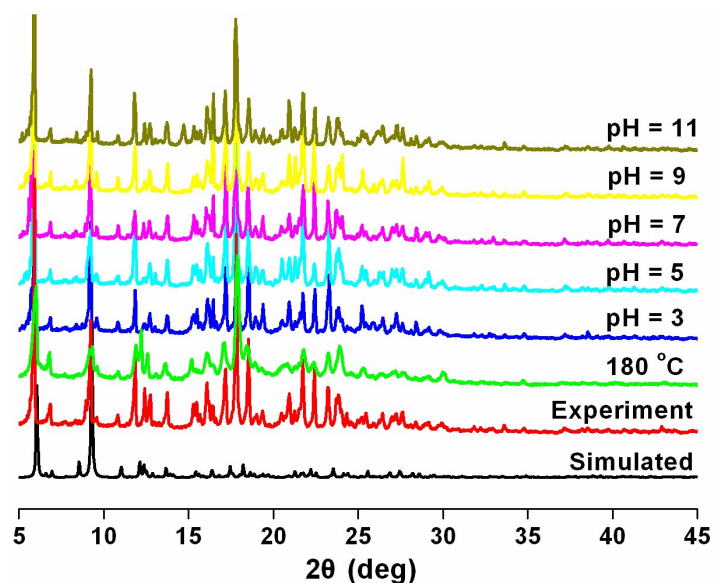
Figure S3. PXRD patterns of the simulated and experimental **Zn-MOF**, activated-**Zn-MOF** and **Zn-MOF** after immeresing in aqueous solution at pH = 3, 5, 7, 9, 11 (24 h).
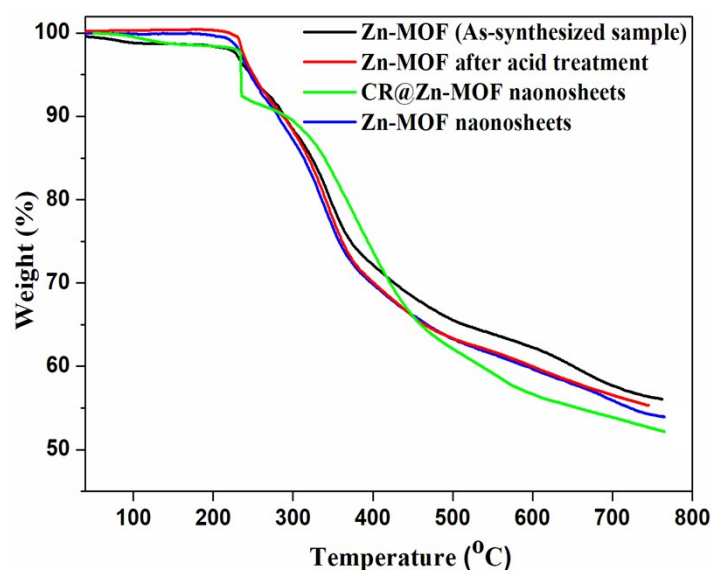
Figure S4. TGA curves of **Zn-MOF**, the protonated **Zn-MOF**, **CR@Zn-MOF** nanosheets and 2D **Zn-MOF** nanosheets. By comparison of the TGA curves for different samples, it can be seen that the three samples of **Zn-MOF**, the protonated **Zn-MOF** and 2D **Zn-MOF** nanosheets presented similar stability, and they could be stable to 220 °C without obvious weight loss. A slight weight loss (1.9 %) was observed for the **Zn-MOF** in the temperature range of 40-220 °C, corresponding to the loss of guest molecules in the framework. For **CR@Zn-MOF** nanosheets, a steep decrease of weight loss was obtained for **CR@Zn-MOF** nanosheets when the temperature above 225 °C, which can be attributed to the departure of CR molecule as a result of the relative weak interaction (such as electrostatic attraction and hydrogen bonding) with **Zn-MOF** nanosheets.
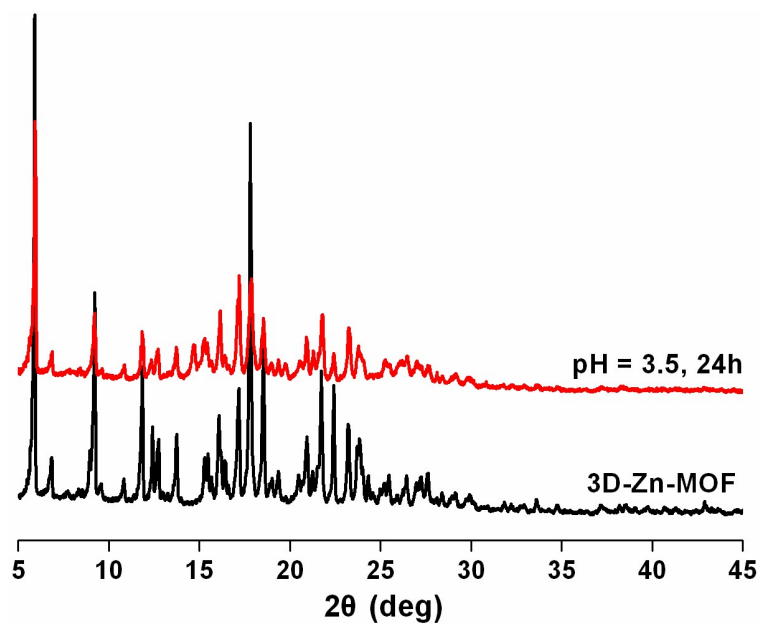
Figure S5. PXRD patterns of 3D bulk **Zn-MOF** and 3D nano-**Zn-MOF**.

(a)	(b)
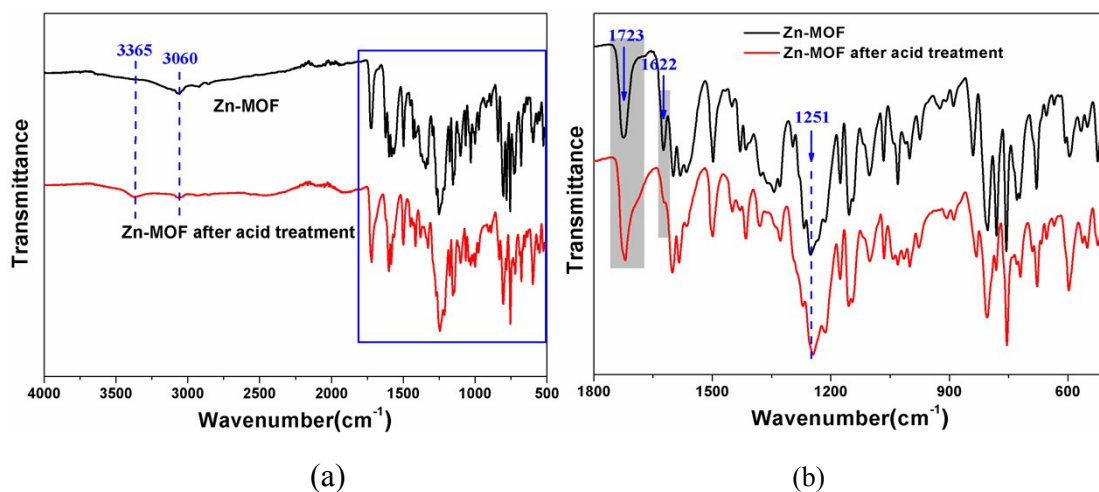
Figure S6. A comparison of the FT-IR spectra of between **Zn-MOF** and **Zn-MOF** after acid treatment at 500-4000 cm^{-1} (a) and 500-1800 cm^{-1} (b).
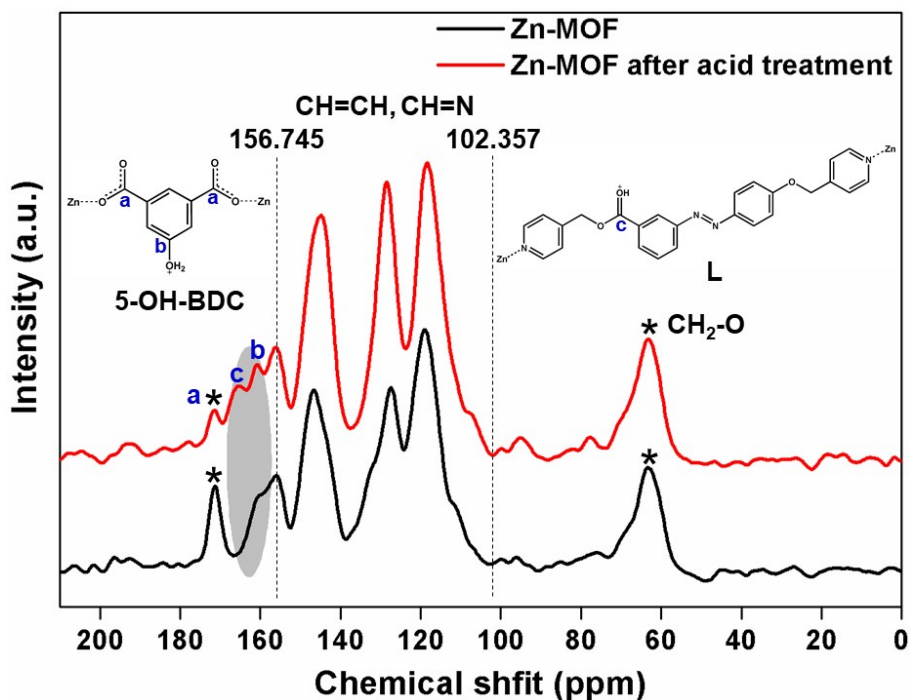
Figure S7. A comparison of the solid state ^{13}C NMR between **Zn-MOF** and **Zn-MOF** after acid treatment. The new appearance of peaks (b and c), confirm the protonation of the hydroxyl and ester groups on **Zn-MOF**. The chemical shifts in the range from 102.357 to 156.745 ppm belong to the peaks of CH=CH and CH=N groups of benzene and pyridine rings in 5-OH-BDC and L ligands. There are many kinds of chemical environment for the ^{13}C element in **Zn-MOF**, owing to the complicated structure of 5-OH-BDC and L ligand. The relatively wide band of the solid state NMR made the peaks of ^{13}C element with different chemical environments cluster together, which can't be separated from one another.
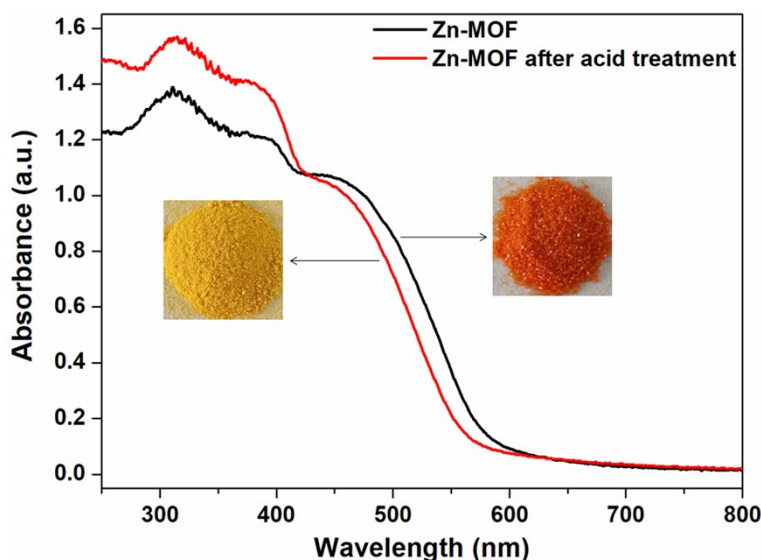
Figure S8. A comparison of the solid UV-vis spectroscopy between **Zn-MOF** and **Zn-MOF** after acid treatment.

(a)   (b)
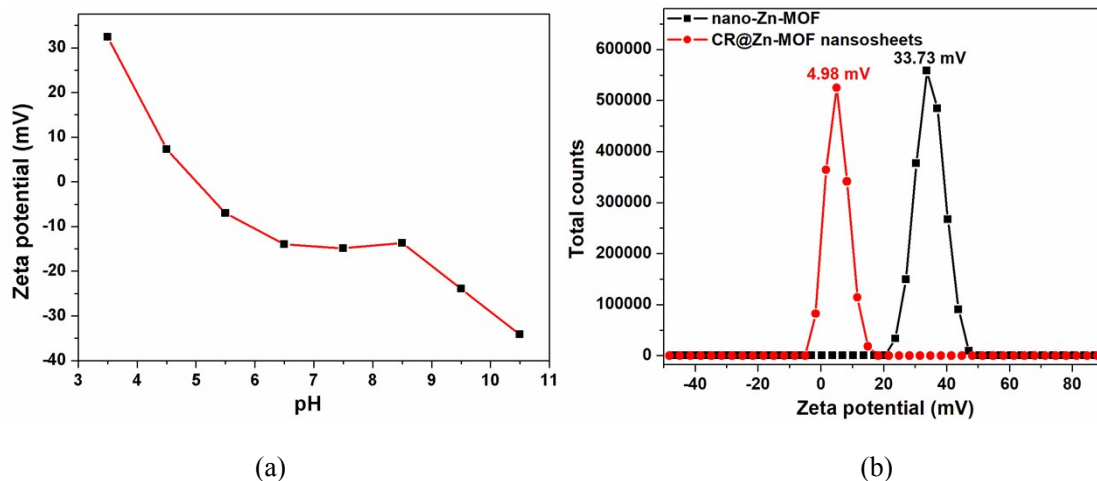
Figure S9. (a) Zeta potential of **Zn-MOF** at different pH values. The considerable functional groups of O–H, C=O, N=N and C–O–C on the MOF maybe act as buffer agent to maintain the solution pH in a relatively stable region, affording the almost unchanged zeta potential in the pH range of 6.5 to 8.5. (b) Zeta potential of **nano-Zn-MOF** and 2D **CR@Zn-MOF** nanosheets.

(a)   (b)
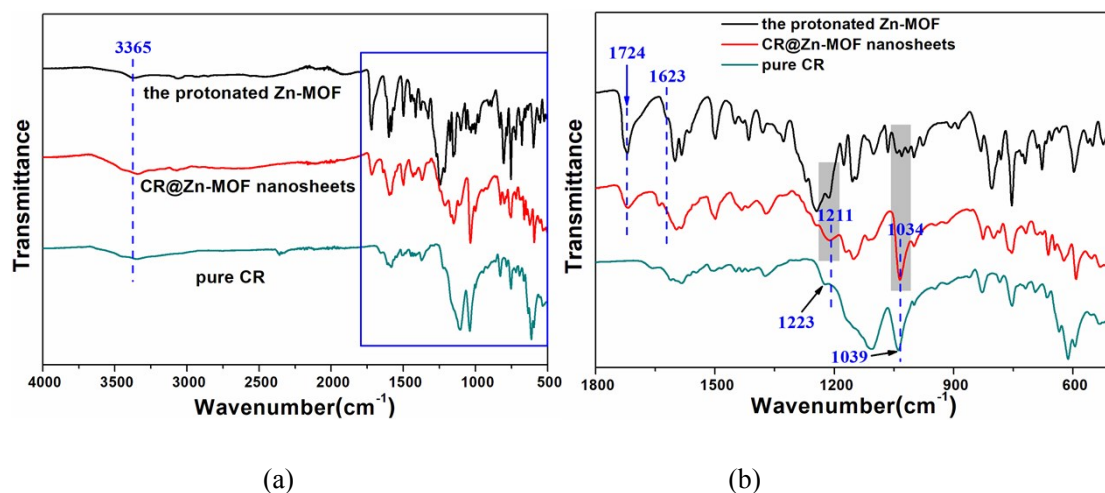
Figure S10. A comparison of the FT-IR spectra of between the protonated **Zn-MOF**, 2D **CR@Zn-MOF** nanosheets and pure CR at 500-4000 cm^{-1} (a) and 500-1800 cm^{-1} (b).
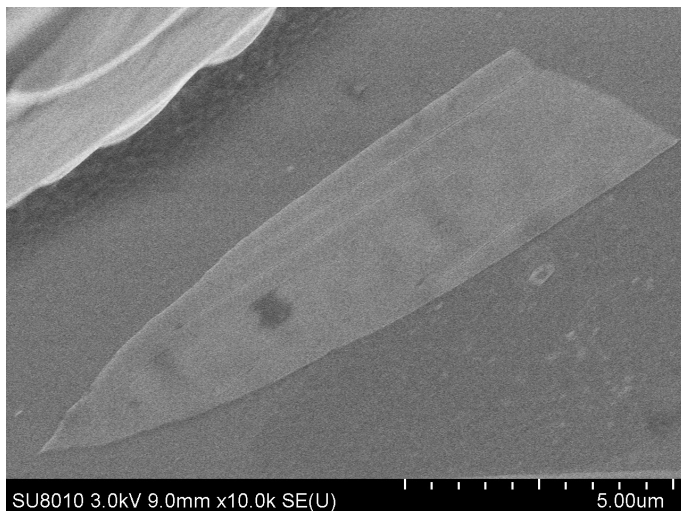
Figure S11. SEM image of 2D **CR@Zn-MOF** nanosheet.
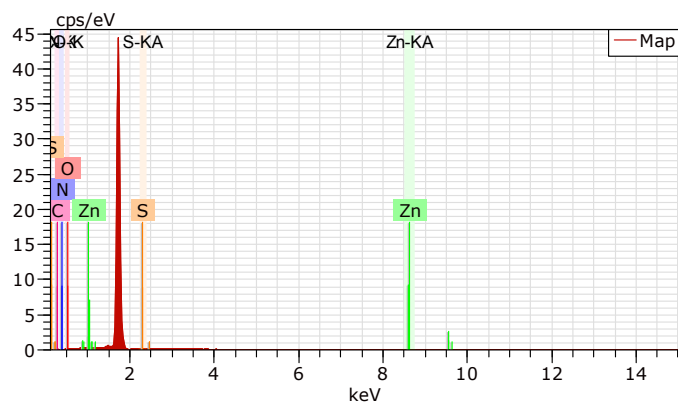
Figure S12. EDS spectrum of 2D **CR@Zn-MOF** nanosheet.
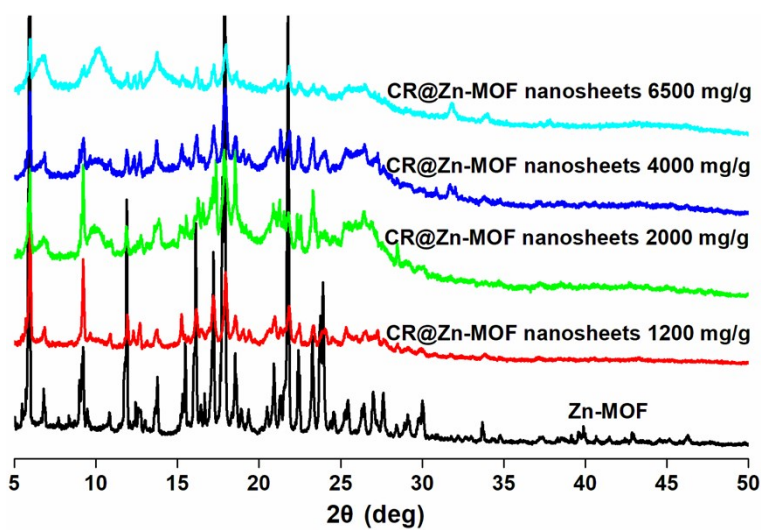
Figure S13. PXRD patterns of **Zn-MOF** and 2D **Zn-MOF** nanosheets with different loaded capacities for CR (1200, 2000, 4000, 6500 mg g^{-1}).
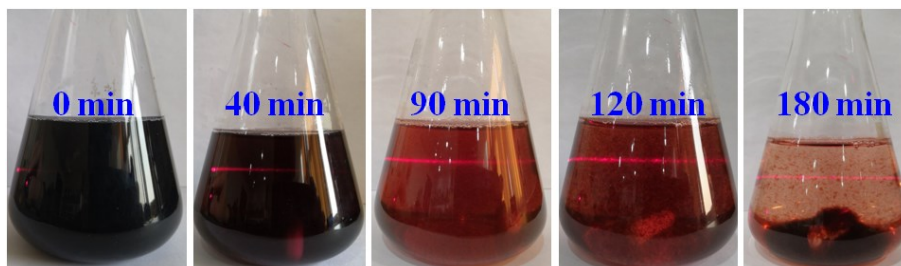
Figure S14. Photograph of the Tyndall effect of 2D **CR@Zn-MOF** nanosheet suspensions for the adsorption and exfoliation process with different times. C_0 = 200 ppm (CR), $m_{nano\text{-}Zn\text{-}MOF}$ = 20 mg, V = 200 mL and pH = 3.5.
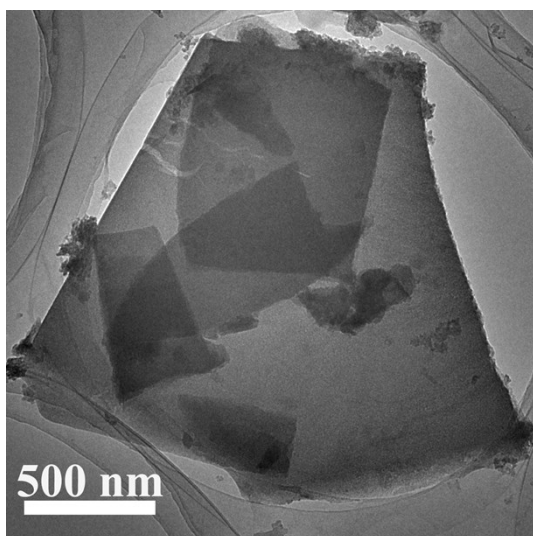
Figure S15. TEM image of 2D **CR@Zn-MOF** nanosheets.
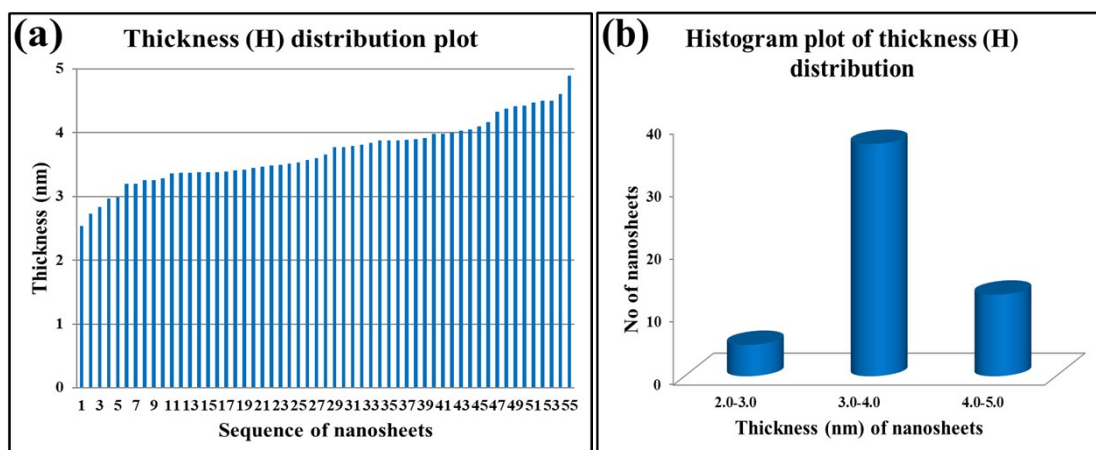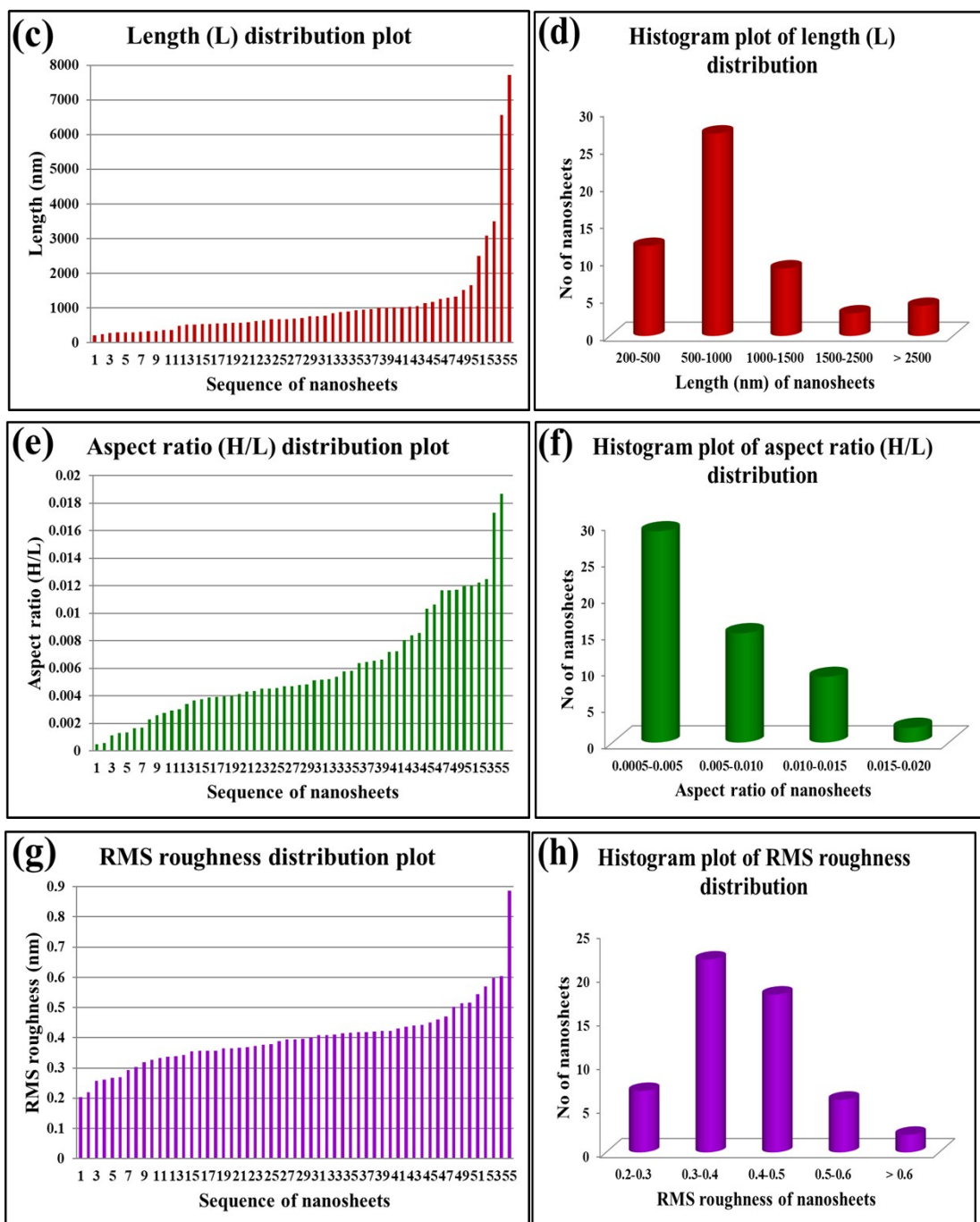
Figure S16. (a) The thickness distribution plot of the exfoliated nanosheets. (b) Histograms of the thickness distribution. Most of the nanosheets have a thickness in the range of 3.0-4.0 nm, which correspond to about single-layer nanosheet (count from single crystal XRD data). (c) Lateral length distribution plot of the exfoliated nanosheets. (d) Histogram plot of lateral length distribution. Most of the nanosheets' lateral dimensions fall within 500-1000 nm. (e) Aspect ratio (H/L) distribution plot of nanosheets. (f) Histogram plot of the aspect ratio distribution. Most of the nanosheets' aspect ratio ranges between 0.0005-0.005. (g) RMS roughness distribution plot of nanosheets. (h) Histogram plot of the RMS roughness distribution. Most of the nanosheets' RMS roughness ranges between 0.3-0.5 nm.
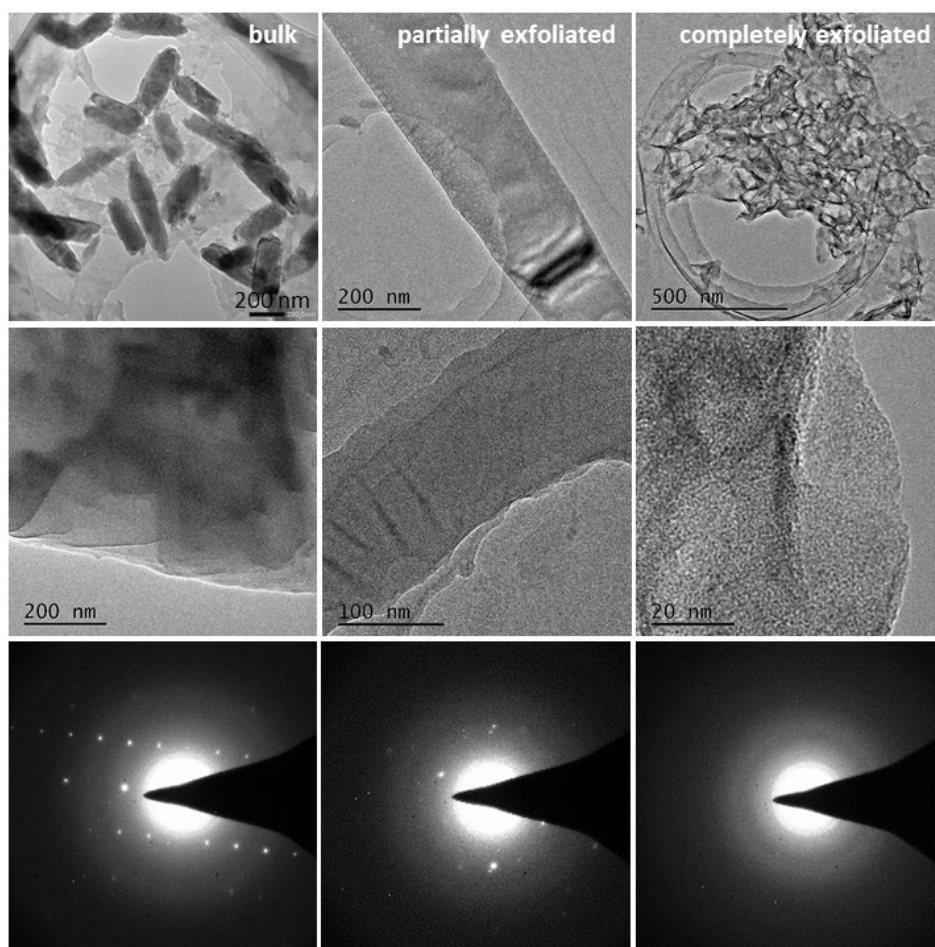
Figure S17. HRTEM images of the highly crystalline bulk **Zn-MOF** and partially exfoliated vs. the well-exfoliated **Zn-MOF** nanosheets. In the SAED patterns, the bulk **Zn-MOF** gave rise to good diffraction, while these partially exfoliated sheets exhibited weaker diffraction and the well-exfoliated nanosheets only showed the presence of highly diffused diffraction rings. This may be due to the lack of sufficient layers and the inherent higher-angle Bragg reflections having very low relative intensities for these MOF monolayers.
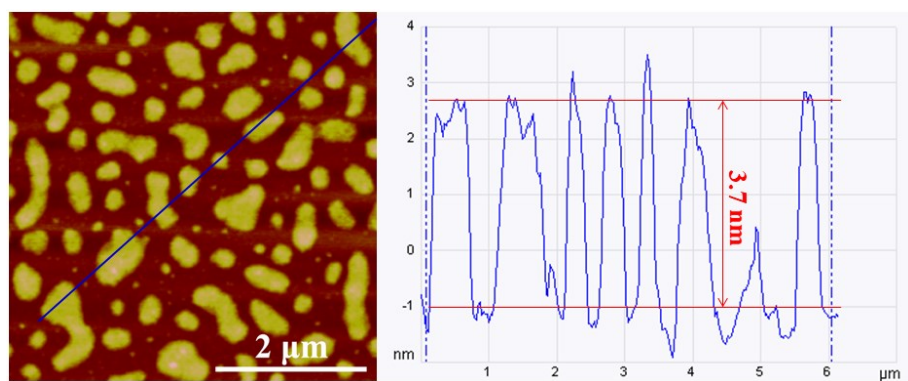
(a)
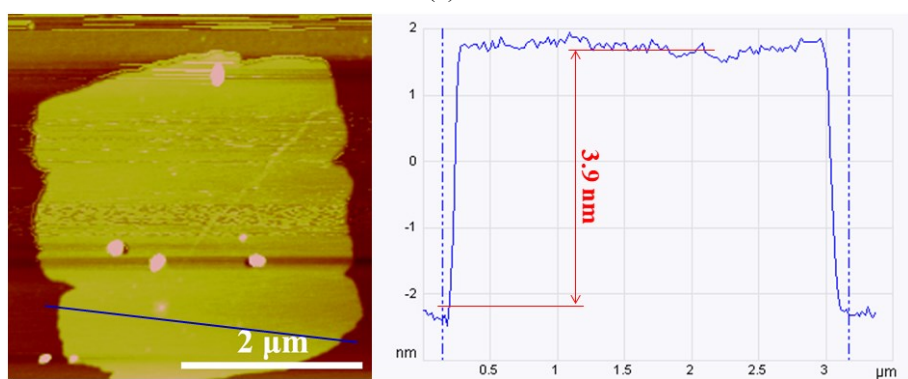
(b)

Figure S18. (a-b) Representative AFM images of 2D **Zn-MOF** nanosheets. The height profile, colour-coded blue, is measured along the corresponding track shown in the AFM.
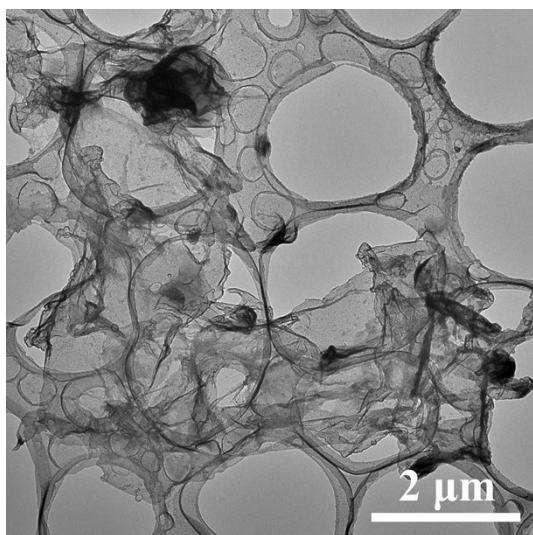
Figure S19. TEM image of a typical 2D **Zn-MOF** nanosheet.
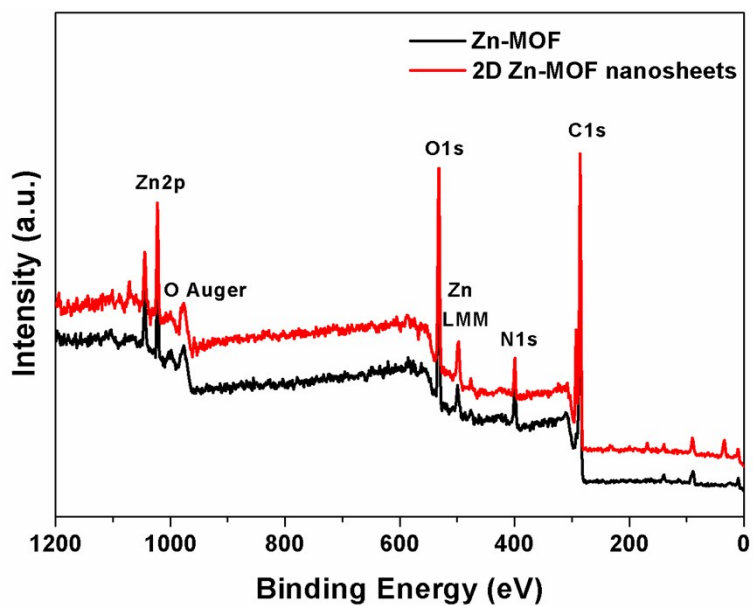
Figure S20. XPS survey spectra of **Zn-MOF** and 2D **Zn-MOF** nanosheets.
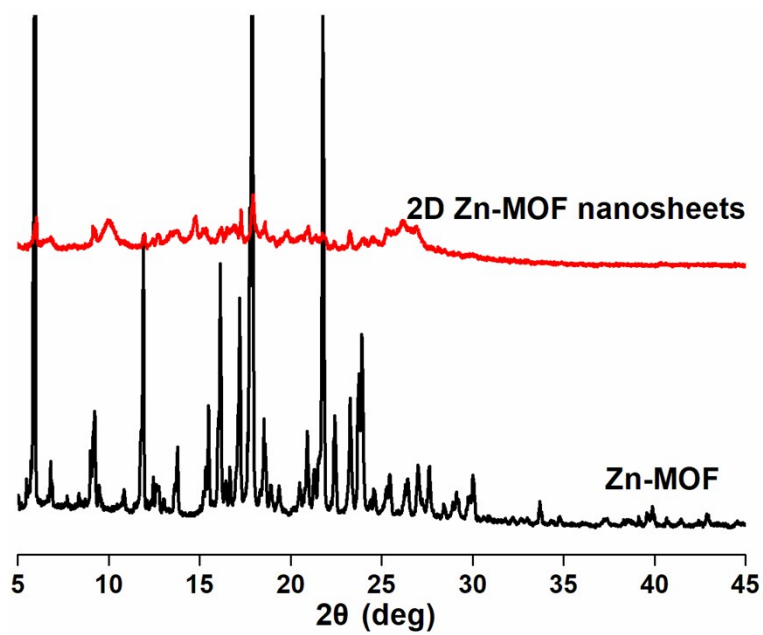
Figure S21. PXRD patterns of **Zn-MOF** and 2D **Zn-MOF** nanosheets.
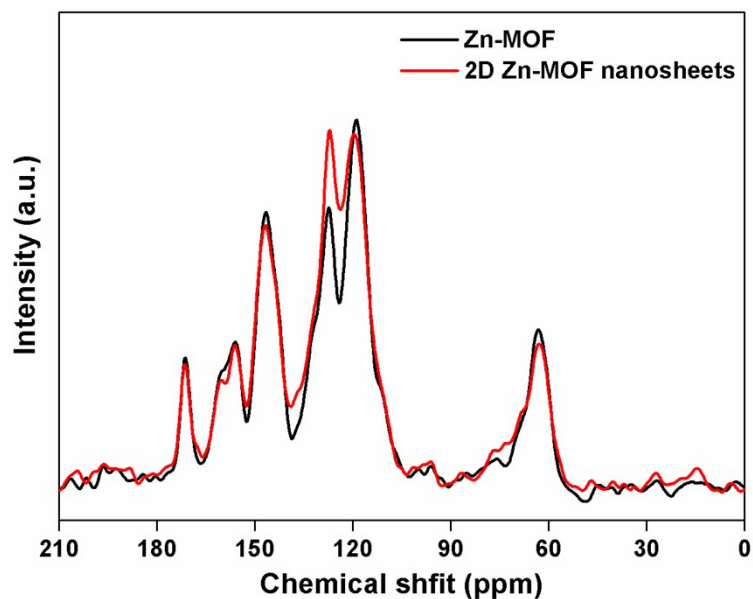
Figure S22. A comparison of the solid state ^{13}C NMR between **Zn-MOF** and 2D **Zn-MOF** nanosheets.

(a)   (b)
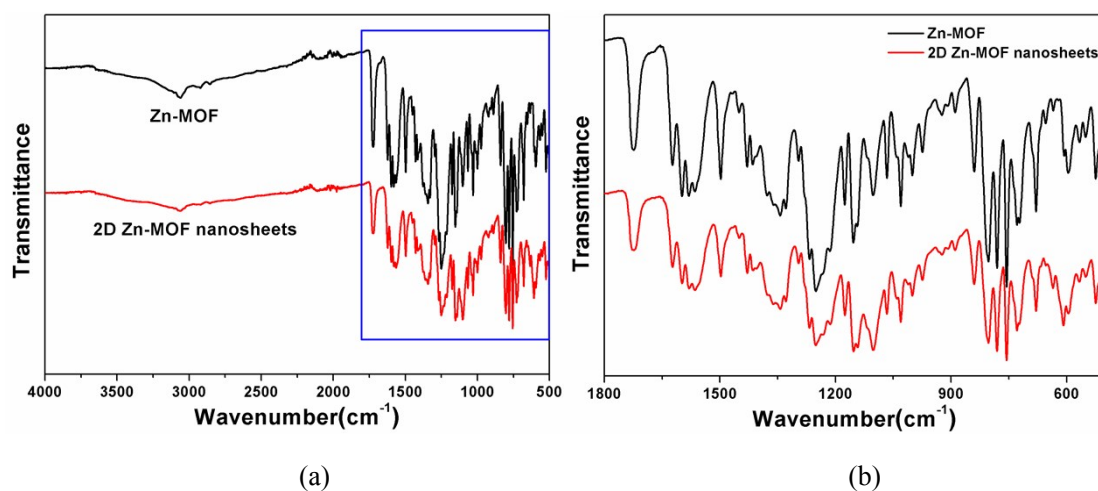
Figure S23. A comparison of the FT-IR spectra of between **Zn-MOF** and 2D **Zn-MOF** nanosheets at 500-4000 cm^{-1} (a) and 500-1800 cm^{-1} (b).
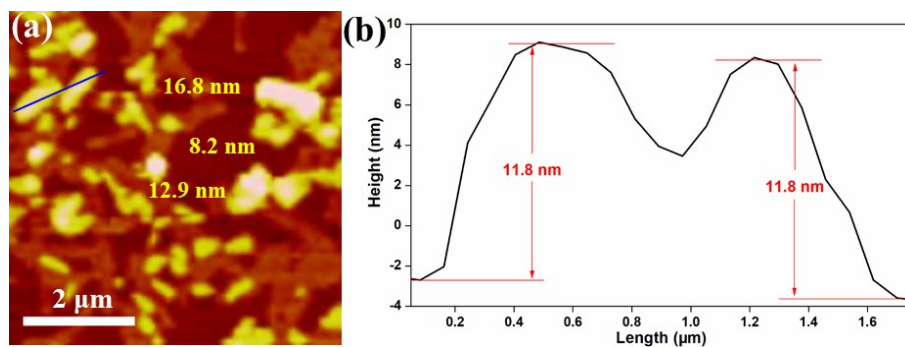
Figure S24. (a) AFM image of the obtained 2D **Zn-MOF** nanosheets by ultrasound method. (b) The height profile, colour-coded blue, is measured along the corresponding track shown in (a).
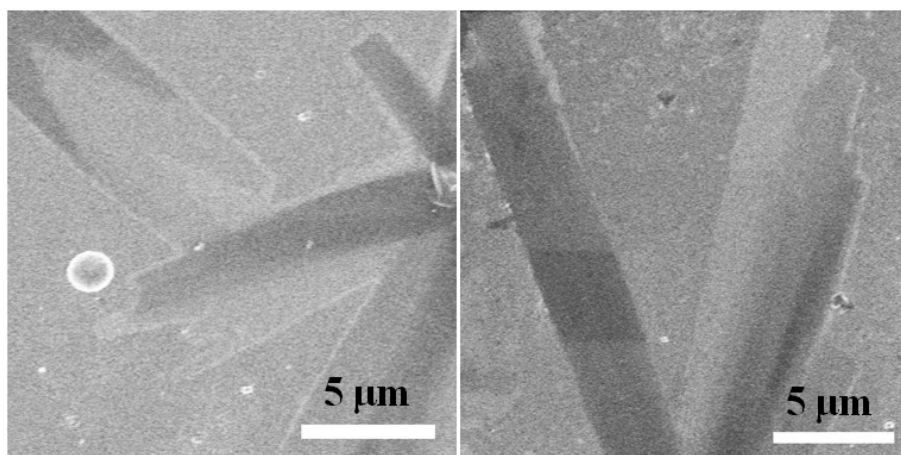
Figure S25. SEM images of 2D **MO@Zn-MOF** nanosheets.
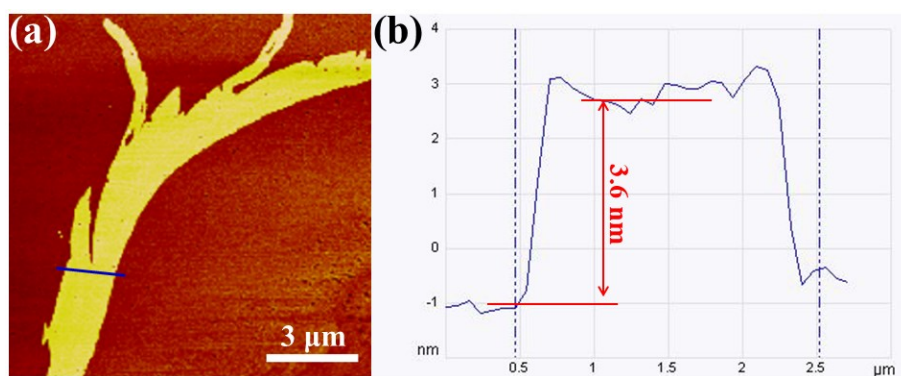
Figure S26. (a) AFM image of 2D **Zn-MOF** nanosheet. (b) The height profile, colour-coded blue, is measured along the corresponding track shown in (a).
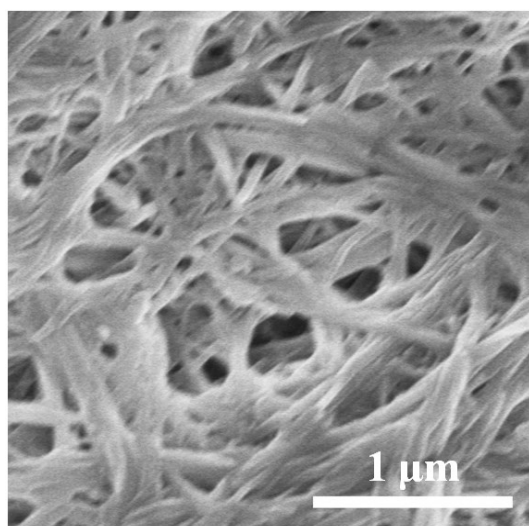
Figure S27. SEM image of 3D layered **Zn-MOF**.
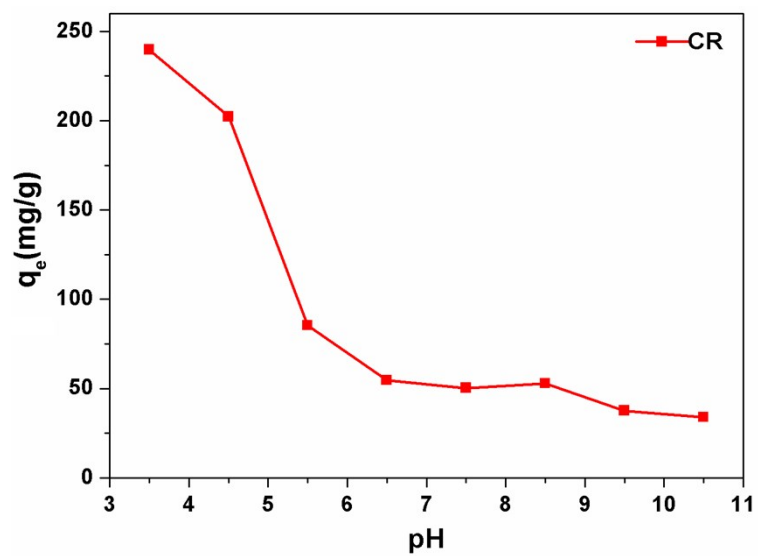
Figure S28. The pH effect on CR adsorption by 2D **Zn-MOF** nanosheets.
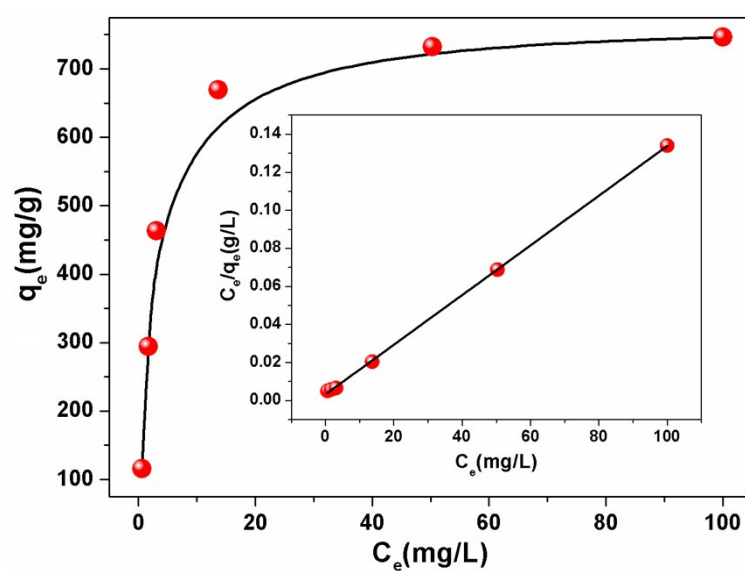
Figure S29. MO adsorption isotherm for 2D **Zn-MOF** nanosheets. Inset: the linear expression fitted with the Langmuir model.
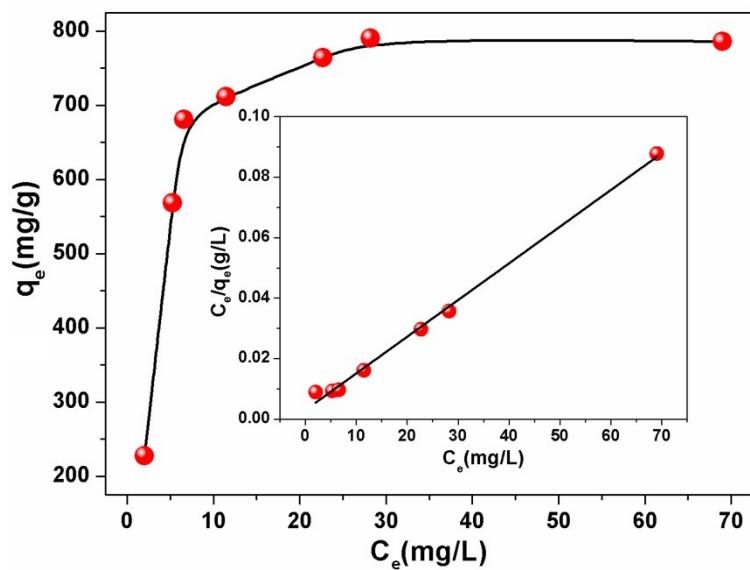
Figure S30. AO adsorption isotherm for 2D **Zn-MOF** nanosheets. Inset: the linear expression fitted with the Langmuir model.
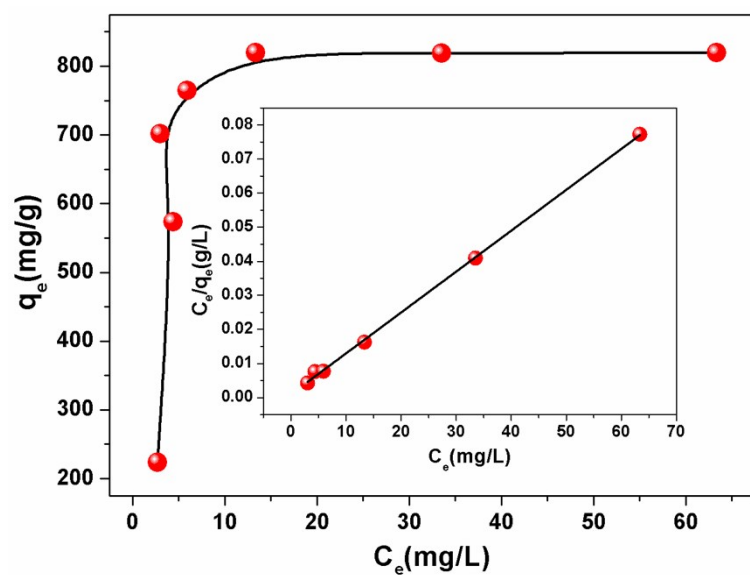
Figure S31. AR adsorption isotherm for 2D **Zn-MOF** nanosheets. Inset: the linear expression fitted with the Langmuir model.
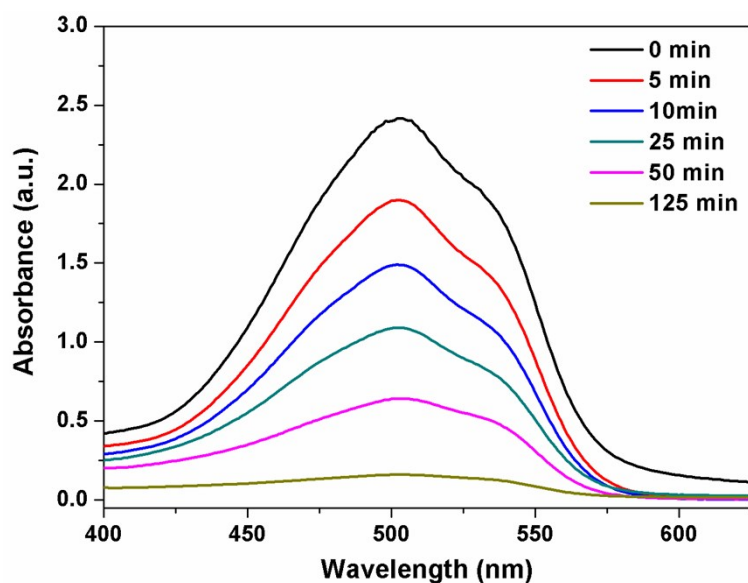
Figure S32. UV-Vis spectral changes of dye mixture (CR&MO&AO&AR) in the presence 2D **Zn-MOF** nanosheets.
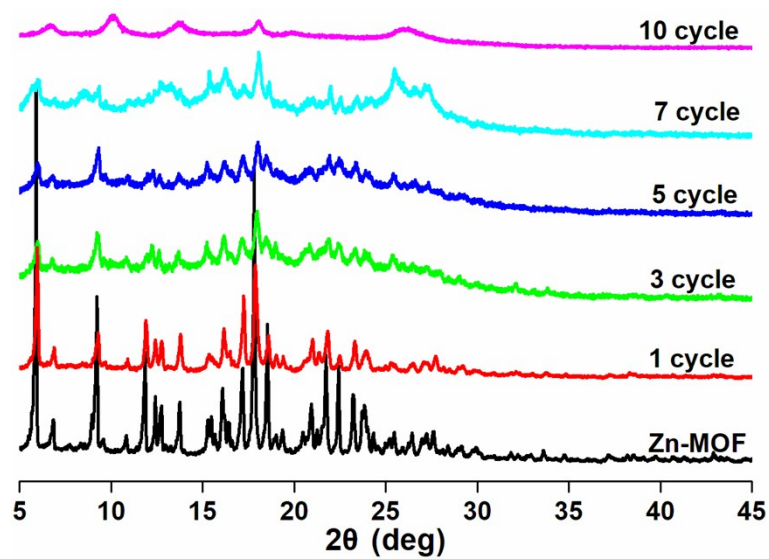
Figure S33. Experimental PXRD patterns of **Zn-MOF** and the recovered samples after 1, 3, 5, 7 adsorption/elution cycles. $C_0 = 300$ ppm (CR), m = 150 mg, V = 150 mL and pH = 3.5.
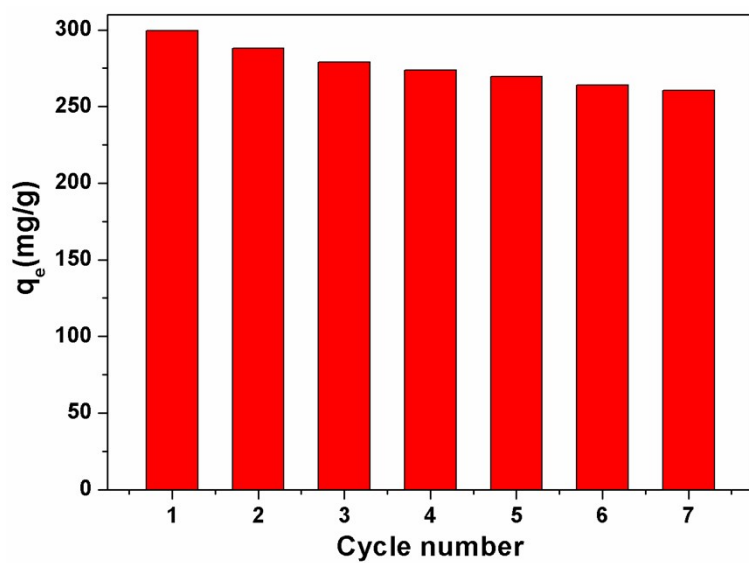
Figure S34. Cycle performance for CR adsorption.
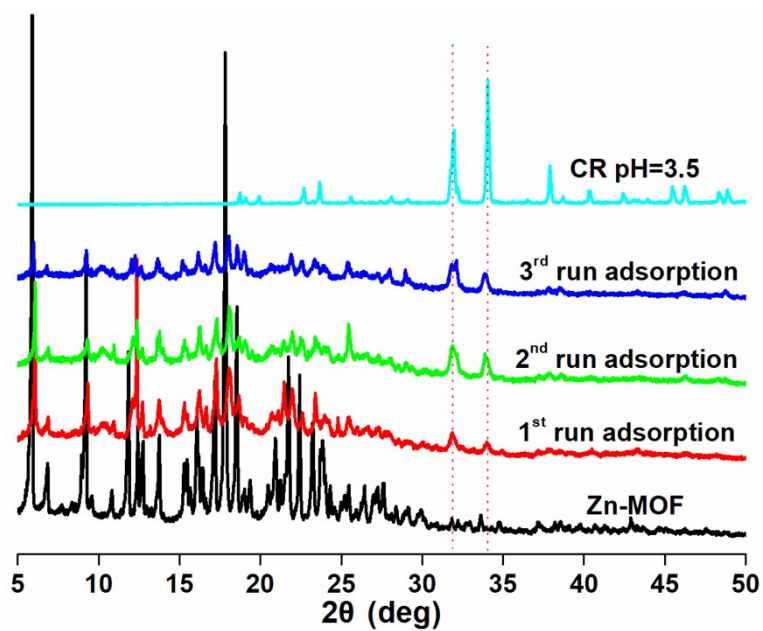
Figure S35. Experimental PXRD patterns of **Zn-MOF** after CR adsorption and pure CR at pH = 3.5.
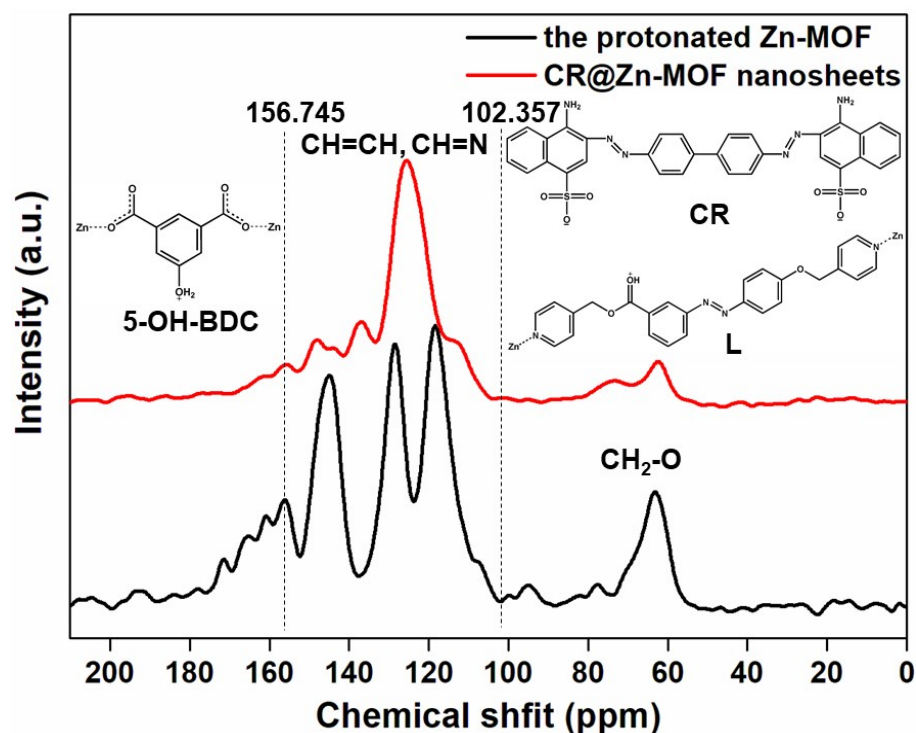
Figure S36. A comparison of the solid state ^{13}C NMR between the protonated **Zn-MOF** and **CR@Zn-MOF** nanosheets. The chemical shifts in the range from 102.357 to 156.745 ppm belong to the peaks of CH=CH and CH=N groups of benzene and pyridine rings in 5-OH-BDC, L ligands and CR. There are many kinds of chemical environment for the ^{13}C element in **CR@Zn-MOF** nanosheets, owing to the complicated structure of L ligand and CR molecule. The relatively wide band of the solid state NMR made the peaks of ^{13}C element with different chemical environments cluster together, which can't be separated from one another.
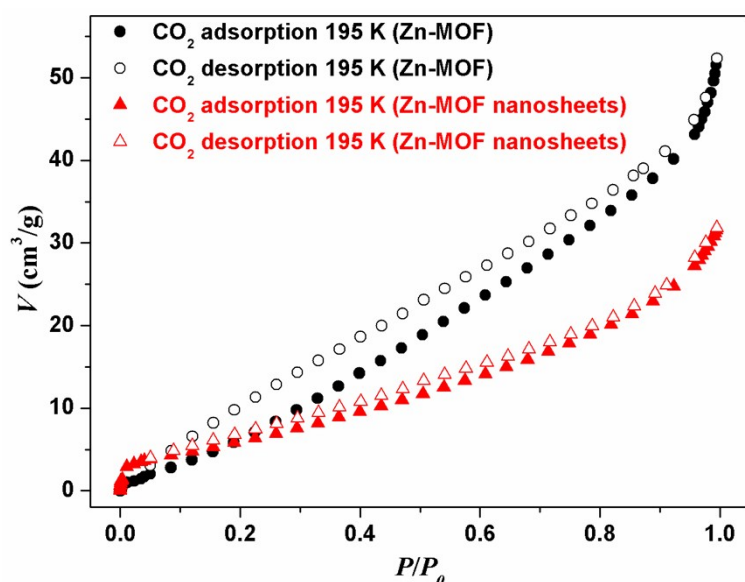
Figure S37. Gas adsorption and desorption isotherms for **Zn-MOF** and 2D **Zn-MOF** nanosheets. The **Zn-MOF** exhibited a BET surface area of *ca.* 38.5 m^2 g^{-1}. The observed low adsorption capacity can be ascribed to the loss of the long-range order under high vacuum for the frameworks,

and the offset-packing of the layers results in the partially blocked pores precluding gas mobility, which generally happens to some highly porous MOFs.[4,5] Compared with the BET surface area of **Zn-MOF**, a noticeable drop was observed for 2D **Zn-MOF** nanosheets. This is because it does not form channels/tunnels as 3D **Zn-MOF** in the *c*-direction,[6] which can be accommodated gas molecules and aids the interaction with gas molecules.

Table S1. Parameters of different isotherm models (298 K) fitting for CR adsorption.

Isotherm models	Parameters			
Langmuir	$q_{m,L}$ (mg g^{-1})		K_L (L mg^{-1})	R^2
	6713.26		0.628	0.999
Freundlich	K_F ((mg g^{-1})/(mg L^{-1})$^{-1/nF}$)		n	R^2
	2026.37		3.067	0.655
D-R	$q_{m,D-R}$ (mg g^{-1})	k_{D-R} (mol^2 J^{-2})	E (kJ mol^{-1})	R^2
	6515.89	1.875×10^{-7}	1.632	0.921

Table S2. Comparison of the maximum adsorption capacities of CR on various adsorbents.

Adsorbents	Maximum adsorption capacity (mg g^{-1})	References
Activated carbon	6.72	7
Mesoporous activated carbon	189.0	8
Chitosan/montmorillonite nanocomposite	54.52	9
Clay materials	20	10
Commercial brucite	90	11
Porous hierarchical MgO	2409	11
Maghemite nanoparticles	208.3	12
Polyvinyl alcohol/melamine-formaldehyde	221.43	13
ZIF-8-M	242	14
TFMOF	252.25	15

Amino-functionalized hierarchical porous SiO$_2$ AlOOH composite nanosheets	506	16
2D LDH nanomaterial	254.14	17
[Co$_3$(tib)$_2$(H$_2$O)$_{12}$](SO$_4$)$_3$	4923.7	18
2D **Zn-MOF** nanosheets	6639.55	this work

Table S3. The pseudo-second-order kinetic parameters of CR for different concentrations.

			Pseudo-second-order kinetics		
T (K)	C_0 (mg L^{-1})	$q_{e,\,exp}$ (mg g^{-1})	k_2 (g mg^{-1} min^{-1})	$q_{e,\,cal}$ (mg g^{-1})	R^2
298	60	358.86	0.0171	357.14	0.999
	150	898.38	0.0148	900.90	0.999
	300	1797.30	3.538×10^{-4}	1825.92	0.998

Table S4. Adsorption constants of Langmuir isotherm model fitting for MO, AO and AR.

	q_m (mg g^{-1})	K_L (L mg^{-1})	R^2
MO	769.23	0.396	0.999
AO	826.45	0.406	0.995
AR	833.33	1.227	0.998

References

1. L. L. Liu, C. X. Yu, J. M. Du, S. M. Liu, J. S. Cao and L. F. Ma, Construction of five Zn(II)/Cd(II) coordination polymers derived from a new linear carboxylate/pyridyl ligand: design, synthesis, and photocatalytic properties, *Dalton Trans*, 2016, **45**, 12352-12361.

2. G. M. Sheldrick, *SHELXS-97 and SHELXL-97, Program for X-ray Crystal Structure Solution*, University of Göettingen, Germany, 1997.

3. A. Spek, Single-crystal structure validation with the program PLATON, *J. Appl. Crystallogr.*, 2003, **36**, 7-13.

4. V. K. Maka, A. Mukhopadhyay, G. Savitha and J. N. Moorthy, Fluorescent 2D metal-organic framework nanosheets (MONs): Design, synthesis and sensing of explosive nitroaromatic compounds (NACs), *Nanoscale*, 2018, **10**, 22389-22399.

5. M. J. Dong, M. Zhao, S. Ou, C. Zou and C. D. Wu, A Luminescent Dye@MOF platform: emission fingerprint relationships of volatile organic molecules, *Angew. Chem. Int. Ed.*, 2014, **53**, 1575-1579.

6. S. Haldar, K. Roy, R. Kushwaha, S. Ogale and R. Vaidhyanathan, Chemical exfoliation as a controlled route to enhance the anodic performance of COF in LIB, *Adv. Energy Mater.*, 2019, **9**, 1902428.

7. C. Namasivayam and D. Kavitha, Removal of Congo Red from water by adsorption onto activated carbon prepared from coir pith, an agricultural solid waste, *Dyes and Pigments*, 2002, **54**, 47-58.

8. E. Lorenc-Grabowska and G. Gryglewicz, Adsorption characteristics of Congo Red on coal-based mesoporous activated carbon, *Dyes and Pigments*, 2007, **74**, 34-40.

9. L. Wang and A. Wang, Adsorption characteristics of Congo Red onto the chitosan/montmorillonite nanocomposite, *J. Hazard. Mater.*, 2007, **147**, 979-985.

10. V. Vimonses, S. Lei, B. Jin, C. W. K. Chow and C. Saint, Kinetic study and equilibrium isotherm analysis of Congo Red adsorption by clay materials, *Chem. Eng. J.*, 2009, **148**, 354-364.

11. P. Tian, X. Han, G. Ning, H. Fang, J. Ye, W. Gong and Y. Lin, Synthesis of porous hierarchical MgO and its superb adsorption properties, *ACS Appl. Mater. Interfaces*, 2013, **5**, 12411-12418.

12. A. Afkhami and R. Moosavi, Adsorptive removal of Congo red, a carcinogenic textile dye, from aqueous solutions by maghemite nanoparticles, *J. Hazard. Mater.*, 2010, **174**, 398-403.

13. S. A. Bhat, F. Zafar, A. H. Mondal, A. U. Mirza, Q. M. Rizwanul Haq and N. Nishat, Efficient removal of Congo red dye from aqueous solution by adsorbent films of polyvinyl alcohol/melamine-formaldehyde composite and bactericidal effects, *J. Clean. Prod.*, 2020, **255**, 120062.

14. J. Liu, J. Li, G. Wang, W. Yang, J. Yang and Y. Liu, Bioinspired zeolitic imidazolate framework (ZIF-8) magnetic micromotors for highly efficient removal of organic pollutants from water, *J. Colloid Interface Sci.*, 2019, **555**, 234-244.

15. J. Liu, H. Yu and L. Wang, Superior absorption capacity of tremella like ferrocene based metal-organic framework in removal of organic dye from water, *J. Hazard. Mater.*, 2020, **392**, 122274.

16. Z. Yan, L. Fu, H. Yang and J. Ouyang, Amino-functionalized hierarchical porous SiO2-AlOOH composite nanosheets with enhanced adsorption performance, *J. Hazard. Mater.*, 2018, **344**, 1090-1100.

17. W. Dong, Y. Lu, W. Wang, M. Zhang, Y. Jing and A. Wang, A sustainable approach to fabricate new 1D and 2D nanomaterials from natural abundant palygorskite clay for antibacterial and adsorption, *Chem. Eng. J.*, 2020, **382**, 122984.

18. J. J. Li, C. C. Wang, H. F. Fu, J. R. Cui, P. Xu, J. Guo and J. R. Li, High-performance adsorption and separation of anionic dyes in water using a chemically stable graphene-like metal-organic framework, *Dalton Trans.*, 2017, **46**, 10197-10201.